Research Article

Fabio Rizzo* and Cristoforo Demartino

Pressure modes for hyperbolic paraboloid roofs

https://doi.org/10.1515/cls-2020-0019
Received Aug 17, 2020; accepted Oct 24, 2020

Abstract: This paper presents a study on Singular Value Decomposition (SVD) of pressure coefficients hyperbolic parabolic roofs. The main goal of this study is to obtain pressure coefficient maps taking into account spatial non-uniform distribution and time-depending fluctuations of the pressure field. To this aim, pressure fields are described through pressure modes estimated by using the SVD technique. Wind tunnel experimental results on eight different geometries of buildings with hyperbolic paraboloid roofs are used to derive these pressure modes. The truncated SVD approach was applied to select a sufficient number of pressure modes necessary to reconstruct the measured signal given an acceptable difference. The truncated pressure modes are fitted through a polynomial surface to obtain a parametric form expressed as a function of the hyperbolic paraboloid roof geometry. The superpositions of pressure (envelopes) for all eight geometry were provided and used to modify mean pressure coefficients, to define design load combinations. Both symmetrical and asymmetrical pressure coefficient modes are used to estimate the wind action and to calculate the vertical displacements of a cable net by FEM analyses. Results clearly indicate that these load combinations allow for capturing large downward and upward displacements not properly predicted using mean experimental pressure coefficients.

Keywords: hyperbolic paraboloid roofs, pressure modes, singular value decomposition, wind tunnel tests, cables net

1 Introduction

Cable nets and membrane roofs are tensile structures commonly used to cover large spans as sports arenas and music halls [1–4]. They are very light and widely employed in roof systems requiring only perimetric structural supports. They owe their appeal to lightness, cost-effectiveness, and aesthetics. However, different types of tensile roof systems (*e.g.*, cantilevered roofs [5–7], grandstand roofs [6–8], hanging tensile roofs [9, 10], and cable domes of the Geiger type [11]) are exposed to wind loads and therefore can exhibit large aerodynamic response.

Common cable nets have a hyperbolic paraboloid shape with two orders of parallel cables, upward and downward. The two orders of cables have two different functions, stabilizing and load-bearing, depending on the acting loads. Under gravitational loads, upward cables are load-bearing and downward ones are stabilizing while under wind suction upward actions, the opposite is true. These types of roofs are well-performing in high seismic hazard areas because their mass is very low and fundamental periods very high. On the other hand, due to their lightness, they are sensitive to wind and snow actions [12–15].

Cable net roofs are sensitive to asymmetrical load conditions such as a non-uniform wind or snow distributions. These asymmetrical load conditions may result in overloaded and unloaded areas leading to detrimental effects for cable structures because unloaded cables can lose their tension with an excessive decrease in their stiffness. In contrast, overloaded cables can collapse reaching their material stress limit. The last condition is dangerous because the harmonic steel, commonly employed in cables, is characterized by a brittle behavior.

Concerning the wind action, the proper estimation of the spatial distribution of mean pressure coefficients on the roof surface is pivotal. However, this is not sufficient to capture asymmetrical load combinations given by the not-correlated superposition of load peaks. One of the most severe effects due to the time-depending fluctuation and spatial depending variability is the asymmetrical occurrence of upward and downward load peaks, which makes important to also consider the time-depending fluctuations in the design process. Nowadays, effects induced by random fluctuations of the wind loads are generally neglected [30–33].

The probabilistic approach to estimate maxima and minima [34–38] gives a satisfactory estimation of peak val-

***Corresponding Author: Fabio Rizzo:** Gabriele D'Annunzio University, viale Pindaro 42, 65013, Pescara (Pe), Italy; Email: fabio.rizzo@unich.it
Cristoforo Demartino: Zhejiang University/University of Illinois at Urbana-Champaign Institute (ZJU-UIUC), Zhejiang University, Haining, Zhejiang, China

ues but it does not provide any information about the peak spatial distribution and/or time depending correlation.

In Wind Engineering, different numerical approaches were used to obtain a decomposition of the wind pressure random signal into its time-depending fluctuation and spatial variability. For instance, Proper Orthogonal Decomposition (POD) [38] is commonly applied to investigate the effect of randomly fluctuating wind pressures on roofs. Several applications have shown its satisfactory application, *e.g.*, [38–43]. The POD approach is based on a signal decomposition generally computed with the Singular Value Decomposition (SVD) [44]. In particular, the left singular vector representing the fluctuation information, the singular values matrix that content kinetic energy information and, finally, the right singular vector (a.k.a., pressure modes) containing the spatial distribution of the experimental pressure signals were estimated through SVD. The Truncated Singular Value Decomposition (TSVD) allows storing selected pressure modes to reconstruct the original signal with satisfactory accuracy.

Concerning hyperbolic paraboloid roofs, an extensively experimental wind tunnel campaign was carried out [16–18] and results were incorporated in [19] that fills the existing gap in international codes, *e.g.*, [20–29]. The numerical techniques described above can be applied to experimental pressure fields measured in wind tunnels on paraboloid roofs to investigate the time-depending fluctuation and spatial variability. In particular, these wind tunnel measurements can be used to discuss the importance of asymmetrical pressure distribution that is usually neglected in the design phases.

This paper presents an analysis of random pressure fields on hyperbolic paraboloid roofs based on experimental results given by [16]. The TSVD approach was applied to select a sufficient number of modes necessary to reconstruct the measured values given an acceptable difference. The truncated pressure modes are fitted through a polynomial surface to obtain a parametric form expressed as a function of the hyperbolic paraboloid roof geometry. The superpositions of pressure modes (envelopes) were provided for all eight geometries and used to modify mean pressure coefficients trends. Finally, the polynomial fitting of selected pressure modes is used to estimate envelope and asymmetrical pressure coefficients. Both envelope and asymmetrical pressure coefficient modes are used to estimate the wind action and to calculate the vertical displacements of a cable net by FEM analyses. Results clearly indicate that these load combinations allow for capturing large downward and upward displacements not properly predicted using mean experimental pressure coefficients.

2 Experimental setup and mean pressure coefficients trends

Experimental tests on hyperbolic paraboloid roofs were carried out in the CRIACIV (Inter-University Research Centre on Wind Engineering and Building Aerodynamics) open circuit boundary layer wind tunnel in Prato (Italy) [16–19]. Tests refers to scaled models (scale: 1:100) of buildings covered with hyperbolic paraboloid roofs. The geometrical characteristics of the scaled models are summarized in Figure 1.

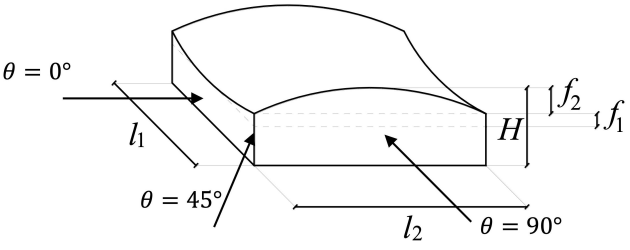

Figure 1: Geometrical characteristics of the scaled models

Tests were performed considering (*i*) four different plan shape (square, rectangular, circular, and elliptical plan) (*ii*) two different curvatures (low and high), and (*iii*) four different total heights. Sixteen different geometries were investigated. The tests were repeated for sixteen wind

Table 1: Geometrical sample, dimensions in m. For the definition of the different variables refer to Figure 1

$\lambda_l = \frac{1}{100}$	G_1	G_2	G_3	G_4	G_5	G_6	G_7	G_8
l_1	80.00	80.00	80.00	80.00	40.00	40.00	40.00	40.00
l_2	80.00	80.00	80.00	80.00	80.00	80.00	80.00	80.00
f_1	2.67	2.67	4.44	4.44	2.67	2.67	4.44	4.44
f_2	5.33	5.33	8.89	8.89	5.33	5.33	8.89	8.89
H	21.33	34.66	26.66	39.99	21.33	34.66	26.66	39.99

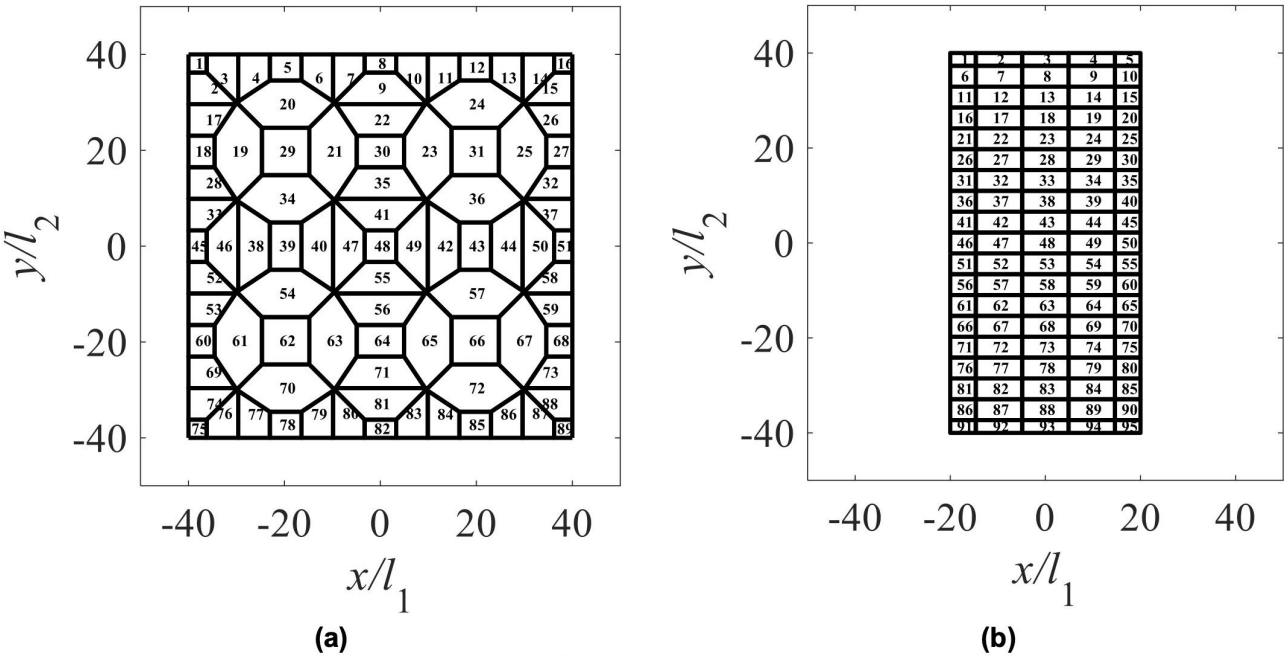

Figure 2: Thiessen polygons for square (a) and rectangular (b) plan roofs

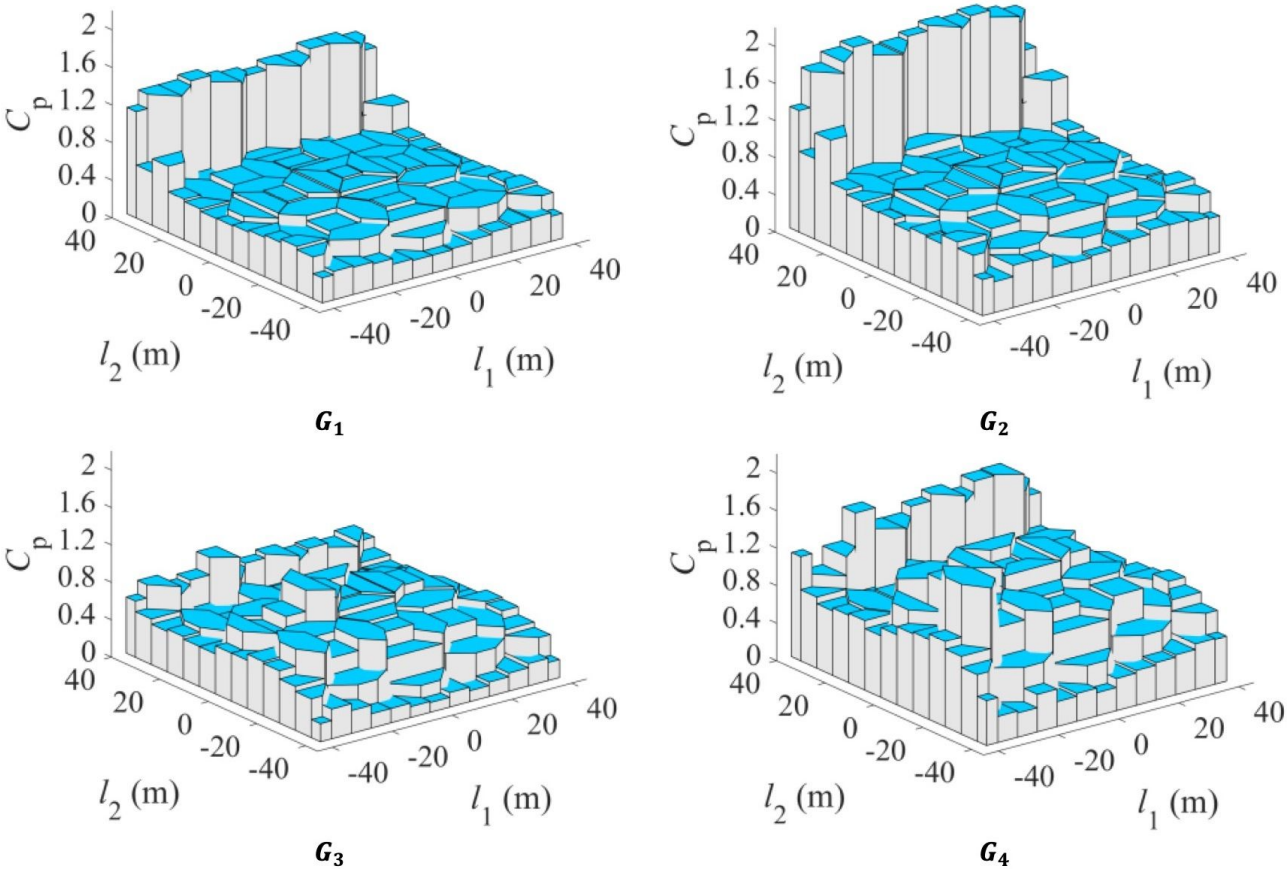

Figure 3: Mean pressure coefficients of square plan geometries with $\theta = 0°$ [16]

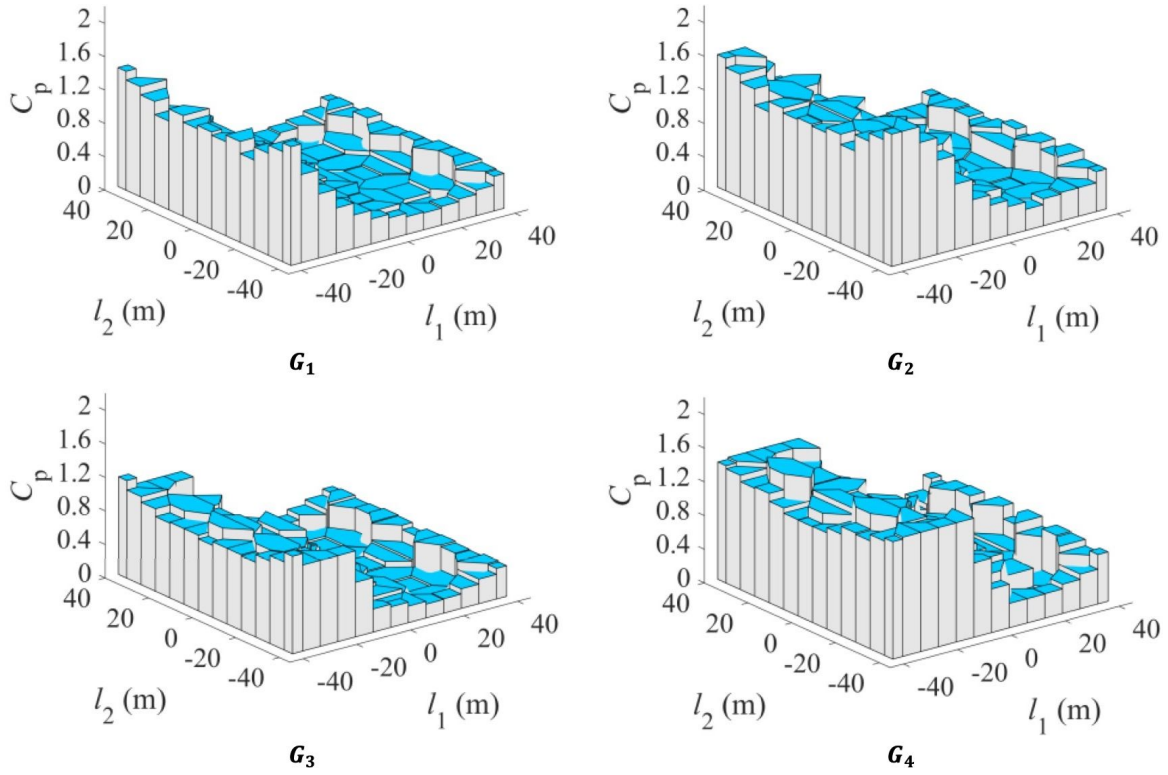

Figure 4: Mean pressure coefficients of square plan geometries with $\theta = 90°$ [16]

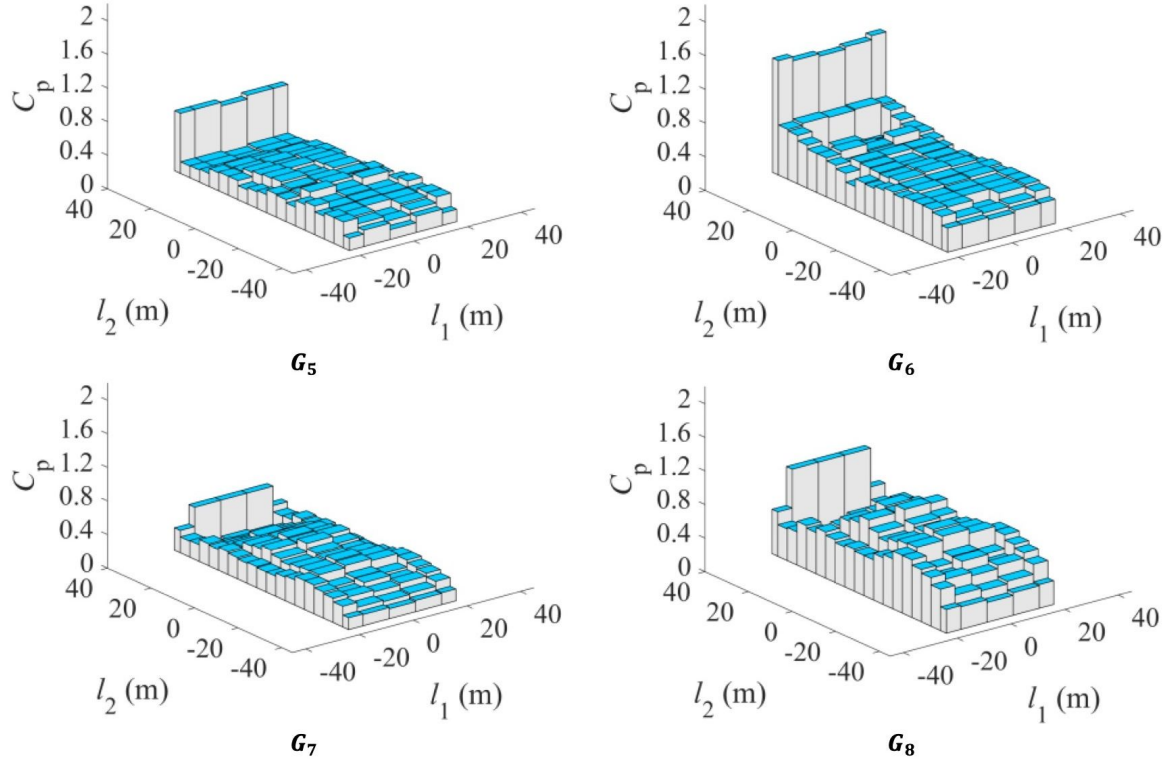

Figure 5: Mean pressure coefficients of rectangular plan geometries with $\theta = 0°$ [16]

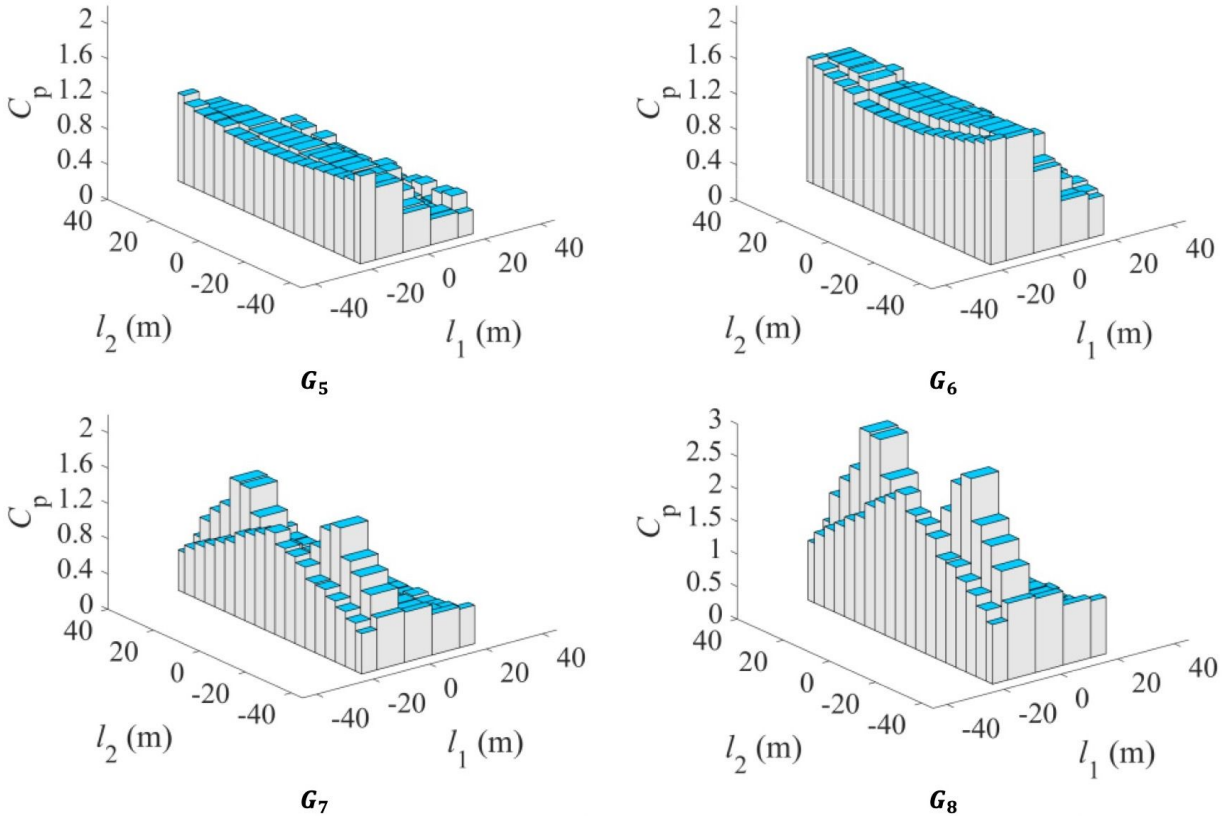

Figure 6: Mean pressure coefficients of rectangular plan geometries with $\theta = 90°$ [16]

angles by rotating the model around the vertical axis in the test chamber.

In the following, only eight different geometries will be used in the analysis: square (*i.e.*, $G_{1...4}$) and rectangular (*i.e.*, $G_{5...8}$) plan shape. Three wind angles will be considered, $\theta = 0°$, 45°, and 90°, respectively. Table 1 gives the geometrical dimensions of the height scaled models. Each model was equipped with 89 pressure-taps for the square plan shape and 95 for the rectangular one.

Experiments were performed with a sampling frequency equal to 252 Hz for a time length equal to 29.77 s (a total of 7504 experimental points for each strain gauge), using a suburban velocity profile [16–18]. The roof surface was divided into Thiessen polygons around each pressure taps assuming constant pressure coefficients for each area. Minima and maxima pressure coefficients were estimated according to [34–38]. Figure 2 shows pressure taps distributions on the square (*i.e.*, 89 pressure taps) and rectangular (*i.e.*, 95 pressure taps) plan roofs.

A summary of the mean pressure coefficients for the height geometries (see Table 1) is reported in Figures 2-5. In particular, Figures 3 and 4 show the pressure coefficients distribution of square plan geometries (*i.e.*, $G_{1...4}$) for $\theta = 0°$ (Figure 3) and 90° (Figure 4). Similar considerations apply to the case $\theta = 45°$; accordingly, this case is omitted in the following for sake of brevity. Figures 5 and 6 show the pressure coefficients distribution of rectangular plan geometries (*i.e.*, $G_{5...8}$) for $\theta = 0°$ (Figure 5) and 90° (Figure 6). Henceforth, positive pressure coefficients indicate suction (*i.e.*, upward action). The interested reader is referred to [16] for a detailed description of the methods and results reported in Figures 3–6 and also for the case $\theta = 45°$.

3 Singular value decomposition of experimental pressure coefficients fields

3.1 Methodology

In linear algebra, the Singular Value Decomposition (SVD) of a matrix is a factorization of that matrix into three matrices. This value has some interesting algebraic properties and conveys important geometrical and theoretical insights about linear transformations. It also has some important applications in data science [38–43]. SVD takes a

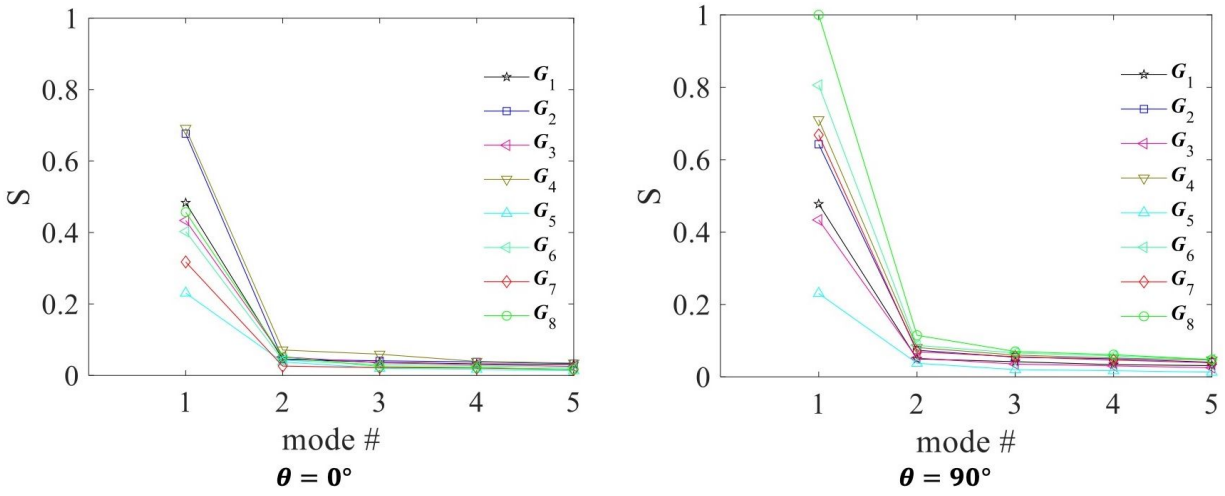

Figure 7: Normalized S estimated using [46] for the first five for all geometries listed in Table 1 and for $\theta = 0°$ (left) and $\theta = 90°$ (right)

rectangular matrix defined as A, where A is a $n \cdot p$ matrix in which the n rows represent the discrete time steps, and p columns each pressure tap [45]. The SVD theorem states:

$$A_{n\cdot p} = U_{n\cdot n} \cdot S_{n\cdot p} \cdot V^T_{p\cdot p} \tag{1}$$

where the $U_{n\cdot n}$ columns are the left singular vectors; $S_{n\cdot p}$ has singular values and is diagonal (mode amplitudes); and $V^T_{p\cdot p}$ has rows that are the right singular vectors [44].

Calculating the SVD consists of finding the eigenvalues and eigenvectors of $A_{n\times p} \times A^T_{n\cdot p}$ and $A^T_{n\cdot p} \cdot A_{n\cdot p}$. The eigenvectors of $A^T_{n\cdot p} \cdot A_{n\cdot p}$ make up the columns of $V_{p\cdot p}$, the eigenvectors of $A_{n\cdot p} \cdot A^T_{n\cdot p}$ make up the columns of $U_{n\cdot p}$. The singular values in $S_{n\times p}$ are also square roots of eigenvalues from $A_{n\cdot p} \cdot A^T_{n\cdot p}$ or $A^T_{n\cdot p} \cdot A_{n\cdot p}$. The singular values are the diagonal entries of the $S_{n\cdot p}$ matrix and are arranged in descending order. The singular values are always real numbers. If matrix $A_{n\cdot p}$ is a real matrix, then $U_{n\cdot n}$ and $V_{p\cdot p}$ are also real.

The SVD numerical approach is commonly used to compute the Proper Orthogonal Decomposition (POD) modes of a random signal. In POD, fluid variables are written as a linear combination of some global modes [38–43]. The purpose of the analysis is to find the deterministic coordinate function $\phi(x, y)$, which best correlates with all the elements of a set of randomly fluctuating wind, pressure fields. $\phi(x, y)$ maximizes the projection from the randomly fluctuating wind pressure field, $p(x, y)$, to the deterministic function, $\phi(x, y)$.

The singular values matrix, S, is a $[7504 \cdot 89]$ eigenvalue matrix for roof with a square plan and a $[7504 \cdot 95]$ for roof with a rectangular plan. It is a diagonal matrix with a $[89 \cdot 1]$ non-zero values diagonal vector [45].

Each row of S diagonal vector contains information about the kinetic energy of each pressure mode. If the data matrix is real, as it is in this case, the singular value matrix and the eigenvalue matrix are the same. The representation of the normalized S estimated using [46] for the first five modes, is illustrated in Figure 7. It can be seen that for all geometries listed in Table 1 and for two wind angles (*i.e.*, $\theta = 0°$ and $\theta = 90°$), values for the first mode are 6 to 14 times bigger than others.

3.2 Pressure modes spatial distribution

The eigenvector squared matrix, V, is a $[89 \cdot 89]$ matrix for the roof with a square plan and a $[95 \cdot 95]$ for the roof with a rectangular plan [16]. Columns are pressure modes while rows are pressure taps. Figures 8-11 show the first pressure mode for all geometries listed in Table 1, for both $\theta = 0°$and $\theta = 90°$, where v is the i-th pressure mode (a vector $[89 \cdot 1]$ for square plan or $[95 \cdot 1]$ for rectangular plan). As it was expected, the first pressure mode is similar to the mean pressure coefficients illustrated in Figures 2-5. Figures 8-11 show a significant difference between $\theta = 0°$ and $\theta = 90°$ and between roofs with square plan and rectangular plan.

Figures 8a and 8b show a very similar trend indicating that for roof with a square plan, pressure mode #1 is not influenced by the model total height, H (see Figure 1). Similar considerations can be done for Figures 8c and 8d. A similar tendency is noted for $\theta = 90°$ (Figures 9 and 10); this is particular evident for geometries G_1 (Figure 9a) and G_2 (Figure 9b). A negligible difference is noted between geometries G_3 (Figure 9c) and G_4 (Figure 9d). On the other hand, the model curvature affects the pressure mode #1. The comparison between Figures 8a and 8c and Figures 8b

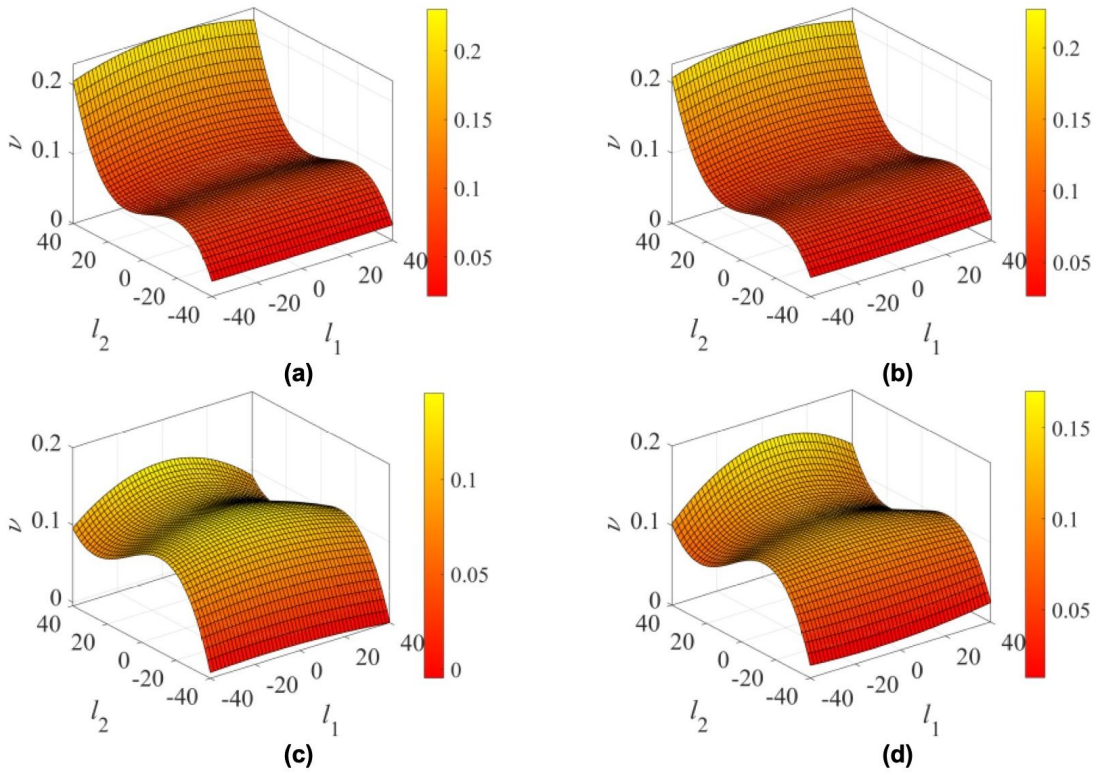

Figure 8: Pressure mode #1 for square plan with $\theta = 0°$ and geometry G_1 (a), G_2 (c), G_3 (b), G_4 (d), referring to Table 1

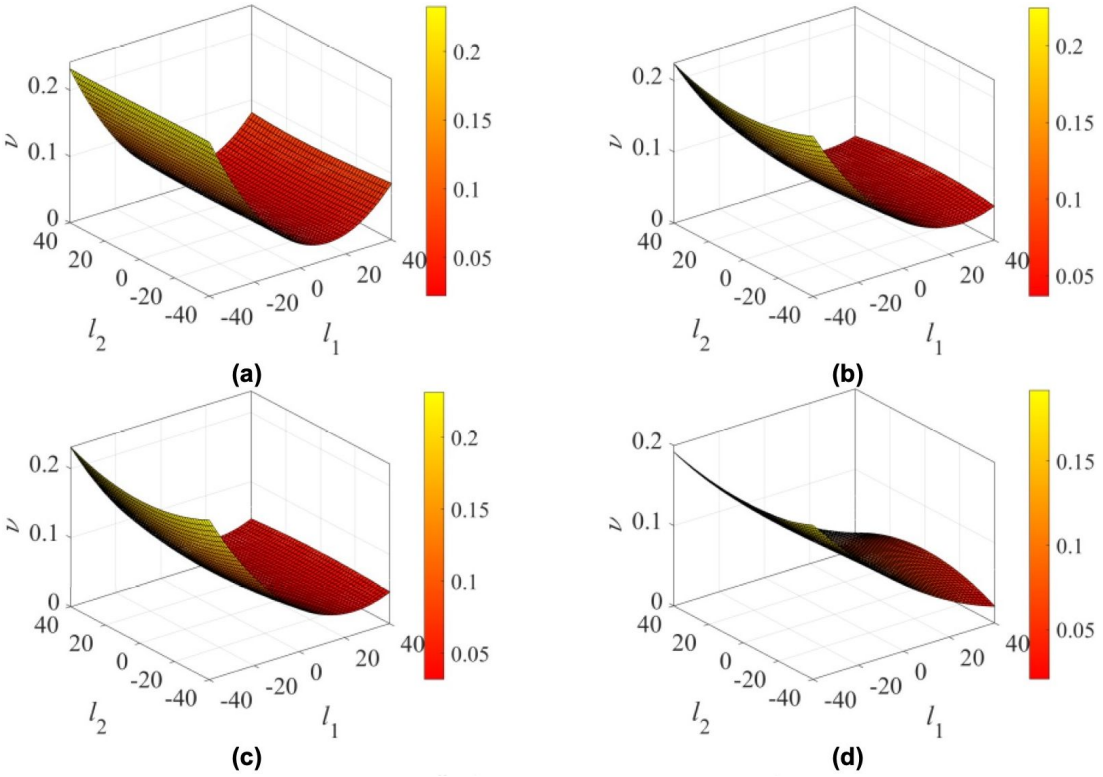

Figure 9: Pressure mode #1 for square plan with $\theta = 90°$ and geometry G_1 (a), G_2 (c), G_3 (b), G_4 (d), referring to Table 1

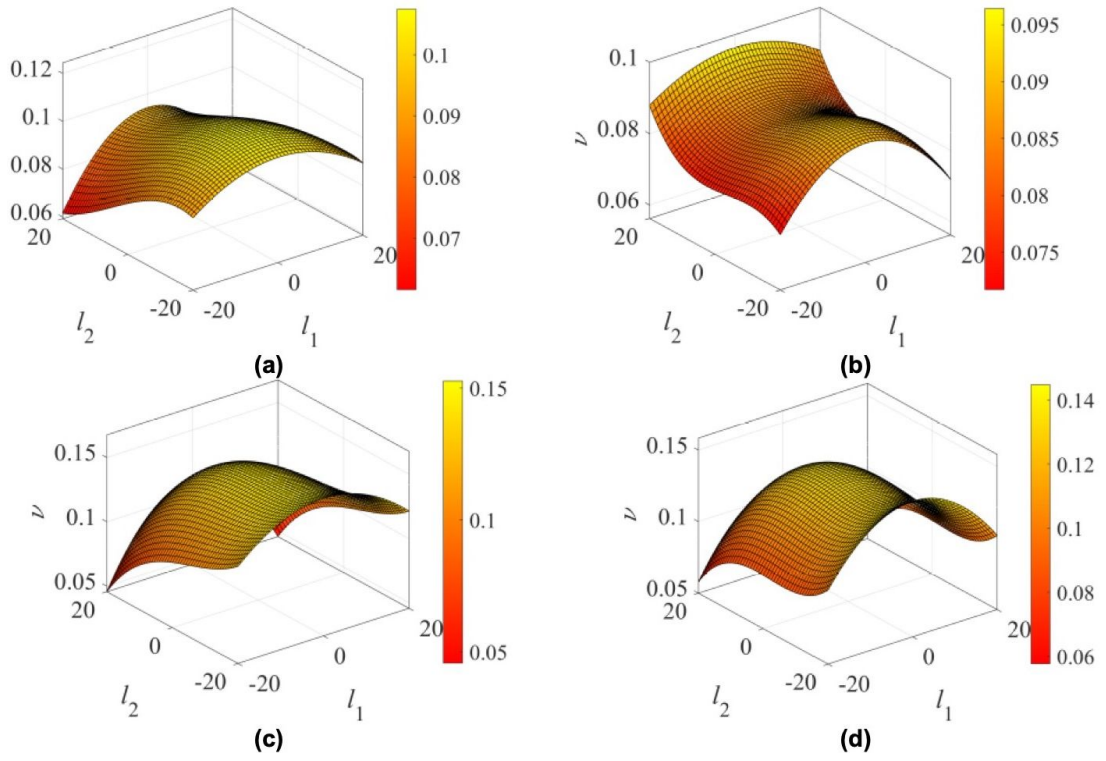

Figure 10: Pressure mode #1 for rectangular plan with $\theta = 0°$ and geometry G_5 (a), G_6 (c), G_7 (b), G_8 (d), referring to Table 1

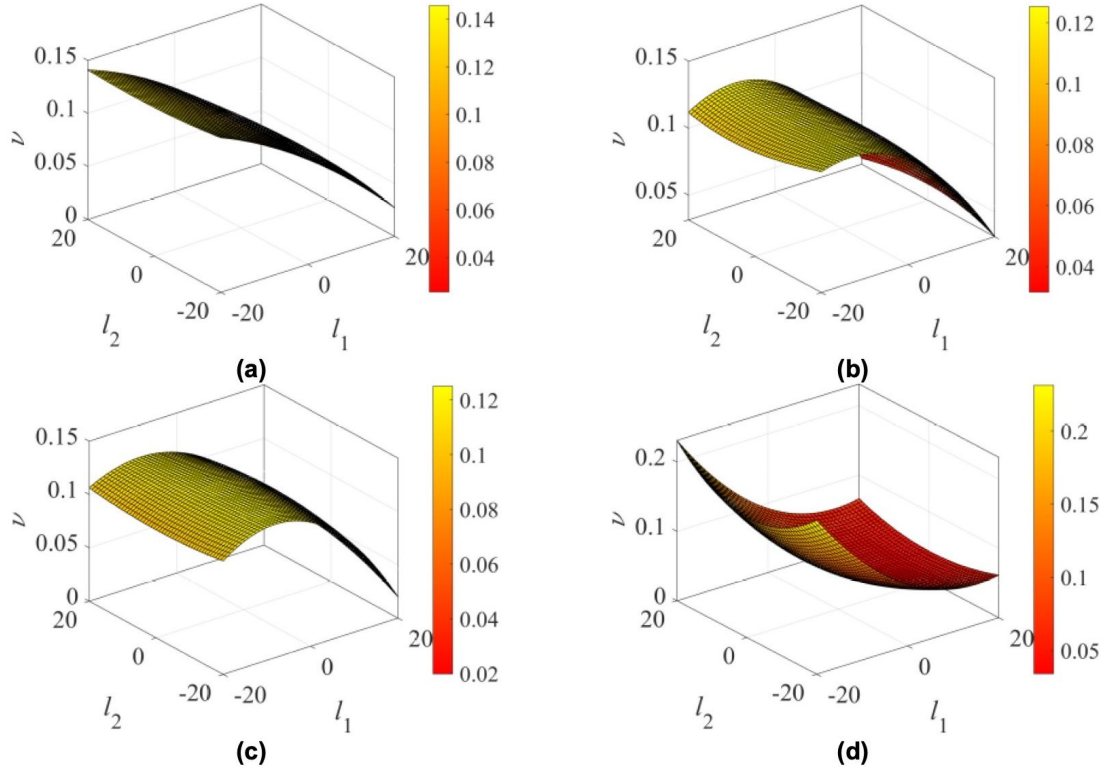

Figure 11: Pressure mode #1 for rectangular plan with $\theta = 90°$ and geometry G_5 (a), G_6 (c), G_7 (b), G_8 (d), referring to Table 1

and 8d shows marked differences in the detachment and the middle of the roof zones.

A significant difference is noted for pressure mode #1 in roofs with a rectangular plan (Figures 10 and 11). In the case of the roof with rectangular plan, the model total height, the roof curvature and the wind angle affect the pressure mode #1 shape. Comparing Figures 9a and 9b a significant difference in the detachment zone is observed. For flatter roofs with rectangular plan shape (G_5 and G_6) the model with a bigger total height, presents larger values of pressure mode #1 in the detachment zone and a valley in the middle of the roof zone (Figure 10b). Differently, when the model has a more curved roof (G_7 and G_8) and a bigger total height, a convexity in the middle of the roof zone is observed (Figure 10d).

A more evident difference is observed between G_7 and G_8, (Figure 11c and Figure 11d) for $\theta = 90°$. G_7 has a total height, H, smaller than G_8 and presents a convex trend (Figure 11c) from the detachment zone. Differently, G_8 shows a concavity along the flow direction (along l_1).

3.3 Envelope of the pressure modes

The upper and lower envelopes are calculated to obtain a synthetic representation of the entire database for square and rectangular plan shapes. For each θ and all normalized pressure modes, an upper and lower envelope was calculated for all eight geometries, as it is illustrated in Figure 12. Specifically, the i-th pressure mode of all eight geometries (Table 1) was overlapped and then the upper and lower surface were selected and finally fitted by a polynomial surface.

Upper and lower pressure mode envelopes were fitted through a 95% level of confidence polynomial surface to obtain a smooth trend as a function of pressure tap locations:

$$\gamma(x,y) = q_1 + q_2x + q_3y + q_4x^2 + q_5xy + q_6x^2 + q_7x^2y + q_8xy^2 + q_9x^3 \quad (2)$$

where $\gamma(x,y)$ is the polynomial surface, $q_1, \ldots, q_9$ are the constants, and x and y are the horizontal axes in the l_1 and l_2 directions (see Figure 1), respectively. The fitting was performed by using the data at each centroid of Thiessen polygons. Two envelopes surfaces (maxima and minima envelopes) were obtained from each i-th pressure mode and they are named ENV # i-th {maxima; minima}. It is noteworthy that eigenvectors (*i.e.*, pressure modes trends) are normalized to 1 and –1 and that they are referred to $\frac{x}{l_1}$ and to $\frac{y}{l_2}$ variable abscise and ordinate.

The following procedure was adopted: pressure modes trends for all eight geometries were normalized in the range from –1 to 1 and they were overlapped (Figure 12); the upper and lower envelopes (ENV # i-th {maxima; minima}) were estimated; the upper and lower envelope surfaces were fitted by a polynomial surface according to Eq. 2; the fitting surfaces were converted as a multiplier, $\gamma(x,y)$, of the experimental mean pressure coefficients (Figures 2-4) as $C_p(x,y) \cdot \gamma(x,y)$. This approach allows to fully preserving the bigger downward or upward ex-

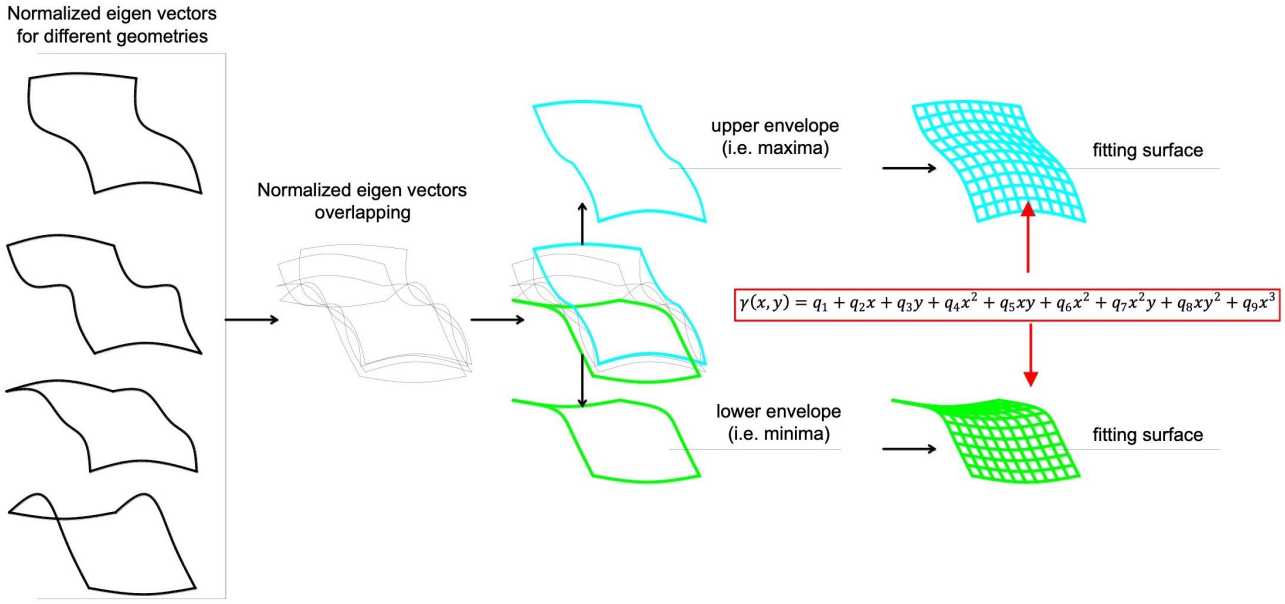

Figure 12: Example of envelope of the maxima and minima Normalized eigenvectors for $\theta = 0°$, pressure mode #1

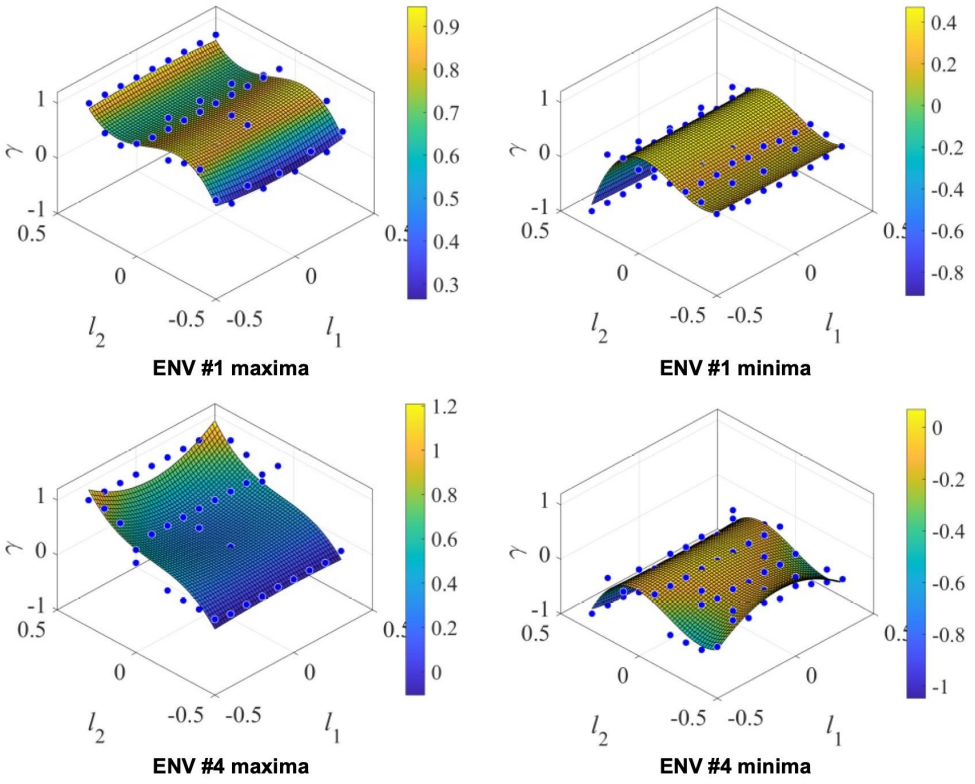

Figure 13: Examples of envelope pressure modes, $\gamma(x, y)$, for $\theta = 0°$

Table 2: Polynomial surface fitting coefficients for envelope pressure modes (Eq. (2), Figure 13)

	ENV									
	maxima					minima				
$\theta = 0°$	#1	#2	#3	#4	#5	#1	#2	#3	#4	#5
q_1	0.80	0.32	0.26	0.30	0.39	0.43	−0.03	0.02	−0.01	−0.08
q_2	0.02	0.04	0.03	−0.04	0.08	0.02	0.01	0.01	0.00	0.05
q_3	−0.91	−1.14	−0.99	−0.12	−0.56	0.69	0.69	0.70	0.35	0.30
q_4	0.19	−0.20	0.31	1.28	1.25	0.08	−0.16	0.01	−1.11	−2.14
q_5	0.00	0.05	0.02	−0.01	0.03	−0.03	−0.01	−0.01	−0.01	0.03
q_6	−1.21	0.55	0.84	0.33	−0.02	−4.88	−2.90	−2.86	−2.98	−2.09
q_7	−1.22	0.02	1.28	3.81	−8.73	0.17	0.46	0.31	4.90	3.64
q_8	−0.20	−0.34	−0.28	0.44	−0.78	−0.19	−0.10	−0.06	−0.02	−0.39
q_9	10.99	14.33	12.97	7.02	14.10	−13.12	−11.26	−11.76	−10.90	−9.78
$\theta = 90°$	#1	#2	#3	#4	#5	#1	#2	#3	#4	#5
q_1	0.81	0.62	0.75	0.81	0.78	0.22	−0.44	−0.56	−0.57	−0.35
q_2	0.04	0.07	0.02	0.01	0.06	0.00	0.06	0.01	0.01	0.04
q_3	0.34	−0.52	−0.56	−0.19	0.36	0.93	0.26	0.71	0.18	0.35
q_4	−1.07	−1.87	−0.56	−1.51	−2.07	0.46	0.92	1.99	0.17	0.40
q_5	0.02	0.07	0.03	0.00	0.02	−0.03	−0.04	0.00	0.01	0.01
q_6	−0.40	1.03	−0.51	−0.82	−0.29	−3.73	−2.42	−2.13	−1.56	−1.76
q_7	−1.40	0.05	1.69	0.06	1.22	−0.26	−5.14	−3.21	0.37	−1.28
q_8	−0.35	−0.50	−0.12	−0.11	−0.55	−0.08	−0.72	−0.12	−0.12	−0.36
q_9	2.75	8.41	7.25	6.47	1.34	−14.29	−4.35	−6.60	−5.66	−6.51

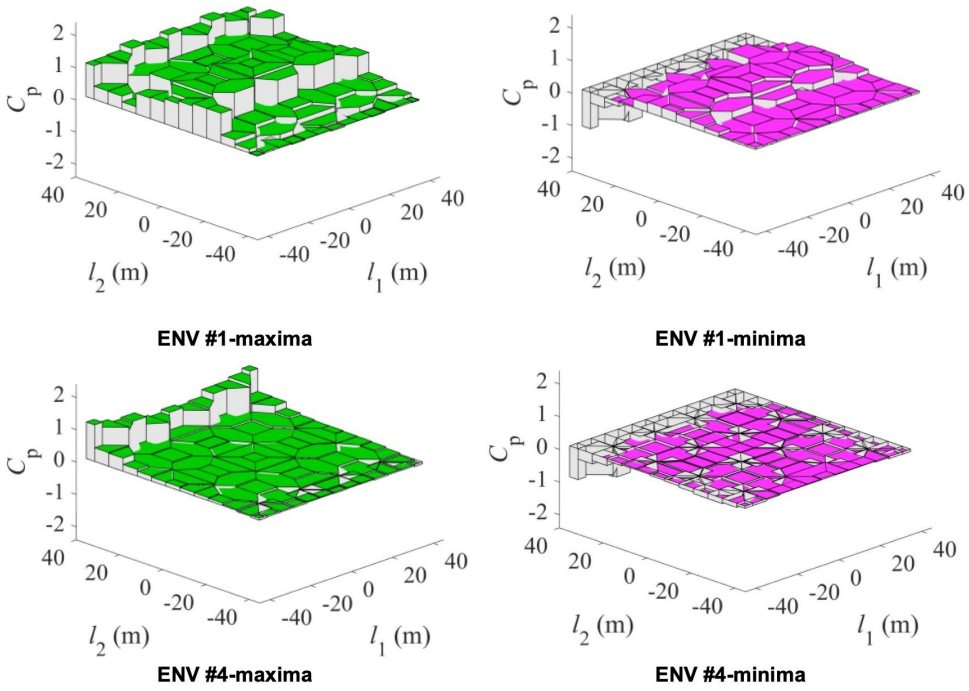

Figure 14: Examples of design pressure coefficient combination, $C_p \times \gamma$, for $\theta = 0°$

perimental values and to reduce values around this with the purpose to obtain a local bigger difference between pressure taps. In the following, the modified pressure coefficients are named envelope pressure coefficients distribution.

Figure 13 shows maximum and minimum envelopes for pressure mode #1 and #4, for geometry G_1 with $\theta = 0°$. Table 2 gives all polynomial coefficients for the first five maxima and minima combinations for $\theta = 0°$ and 90°.

Figure 14 shows two examples of $C_p(x, y) \cdot \gamma(x, y)$ for pressure modes #1 and #4, geometry G_1, and wind angle $\theta = 0°$. Env#1 maxima shows a maximization of pressure coefficients in the middle of the roof zone. On the other hand, ENV#1-minima gives a minimization of pressure coefficients in the middle of the roof zone. The effect of this pressure coefficients trend on the static response of a typical roof with a hyperbolic paraboloid shape, cable net, in terms of vertical displacements corresponds to maxima downwards displacements in this roof zone [47–50].

4 Synthetic representation of the pressure coefficients

4.1 Pressure coefficients reconstruction through the truncated singular value decomposition (TSVD) approach

As discussed in Section 3, the pressure coefficients for one geometry (*i.e.*, [7504 · 89 for square plan roofs) and [7504 · 95] for rectangular plan roofs) can be synthetically described using SVD. In particular, full time-histories can be reconstructed using only the first N pressure modes, according to the TSVD approach. Surrogate pressure coefficients time histories matrix, ${C_p}^S$, (*i.e.*, [7504 · 89], square plan roofs) or [7504 · 95], (*i.e.*, rectangular plan roofs), can be obtained as:

$$ {C_p}^S = U^S \cdot S^S \cdot {V^S}^T \tag{3} $$

where ${V^S}^T$ is the transpose of the surrogate eigenvector matrix reduced to [89 · N] or [95 · N], with the columns corresponding to modes from #1 to N. S^S is the diagonal of the surrogate singular value matrix, reduced to a [89 · N] or [95 · N] vector in which only the first N values are nonzero numbers, corresponding to modes from #1 to #N. The single element (eigenvalue) of S^S is named here λ_m, where m denotes the m^{th} mode. Finally, the surrogate left singular vectors matrix, U^S, is a [7504 · 89] or [7504 · 95] matrix.

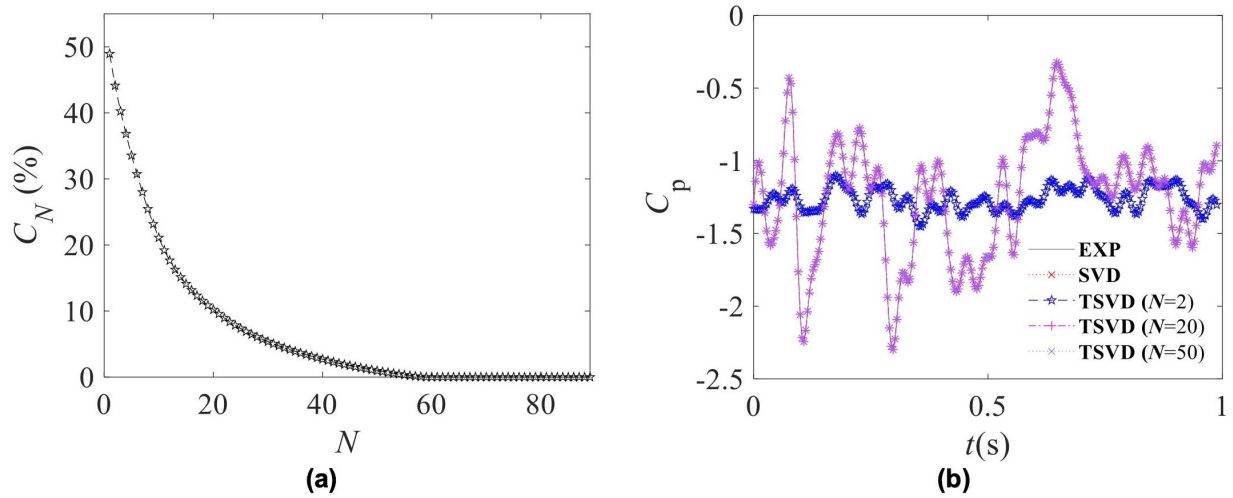

Figure 15: Example of C_N trend (a) and pressure coefficients series by TSVD for the case of geometry G_1, $\theta = 0°$ (b)

The sufficient number of modes for the reconstruction can be estimated by:

$$C_m = \frac{\lambda_m}{\sum_{m=1}^{89,95} \lambda_m} \tag{4}$$

$$C_N = 100 \cdot \left(1 - \sum_{m=1}^{N} c_m\right) \tag{5}$$

where C_m is the proportion of the m^{th} mode, and it denotes the ratio of λ_m to the sum of the eigenvalues, 89 and 95 mean number of pressure taps. C_N is the cumulative proportion, which is the percentage of the error level of the fluctuating wind pressure reconstructed according to Eq. (3), using N modes.

Figure 15a shows an example of the variation of C_N with respect to N for the case G_1, $\theta = 0°$. Figure 15b shows an example of pressure coefficients time history reconstruction by TSVD varying N from 2 to 50. Results show that for $20 \leq N \leq 50$ error level of the fluctuating pressure in percentage is smaller than 10% (Figure 15a). Similar considerations can be done for all geometries and wind angles investigated. It can be concluded that ${C_p}^S$ can be reconstructed using only the first 20 pressure modes having error level of the fluctuating pressure smaller than 10%, which can be considered acceptable to simulate the experimental pressure coefficients time history.

4.2 Synthetic representation of the mean pressure coefficients through the randomization of PSD

A further parametrization of SVD results was computed through the fitting of U^S (*i.e.*, surrogate matrix U obtained by TSVD) columns Power Spectral Density (PSD) with the purpose to store a synthetic representation of matrix U^S. Figure 16a shows an example of the PSD fitting for the case G_1 and $\theta = 0°$. The PSD was fitted according to:

$$PSD(f) = x_1 e^{-x_2 f} + x_3 e^{-x_4 f} \tag{6}$$

where f is the frequency. The coefficients $x_1, \ldots, x_4$ are constant permit to reconstruct U^S. For all pressure taps of each geometry and wind angle, coefficients $x_1, \ldots, x_4$ are fitted through a polynomial surface as a function of x and y coordinates on the roof. This synthetic representation is useful for designers to estimate the PSD of a generic point on the roof. The reconstructed by fitting U^S is named ${U^S}^F$.

Figure 16 shows an example of PSD fitting and Figure 16b shows the variability of the $PSD(f)$ for all pressure taps on G_1 for $\theta = 0$.

In this case, PSD can be used to reconstruct the experimental mean pressure coefficients, $C_{p,mean}$, neglecting phase information. First, $PSD(f)^s$ is converted to amplitude $A(f)$ as:

$$A(f) = \sqrt{2 \cdot PSD(f)} \tag{7}$$

Then, a frequency domain signal $z(f)$ is calculated as:

$$z(f) = A(f)\, e^{[i\varphi(f)]} \tag{8}$$

where $\varphi(f)$ is a random phase in the frequency domain giving each spectral component a random phase uniformly distributed between 0 and 360° and where i is the imaginary number, $i = \sqrt{-1}$. Finally, $z(f)$ is used in the inverse FFT ($IFFT$) algorithm for positive valued (one-sided) functions:

$${U^S}^F = IFFT[z(f)] \tag{9}$$

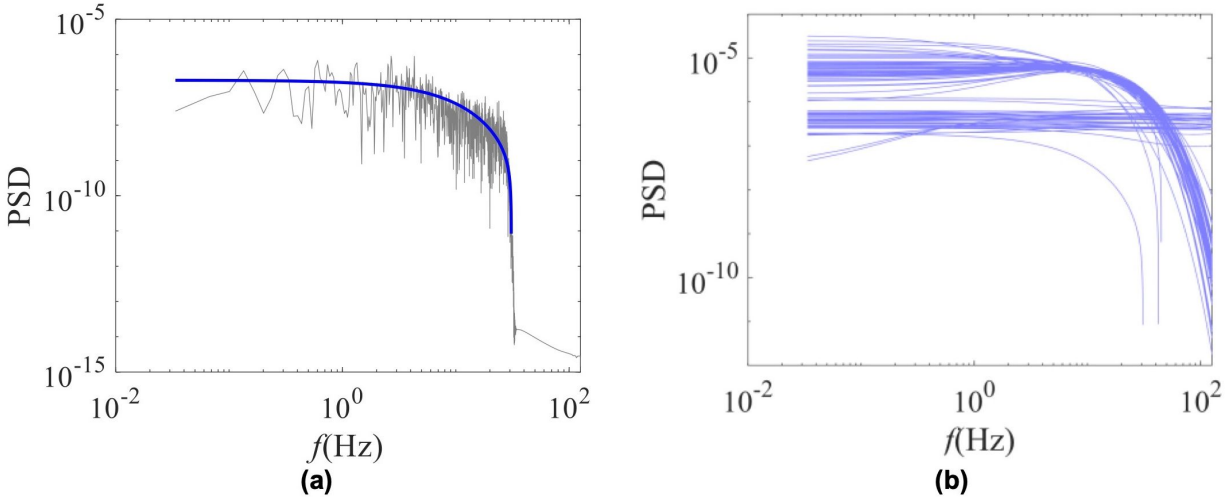

Figure 16: Eigenvalue #1 of the time history (a), and PSD (b). (G_1, $\theta = 0°$)

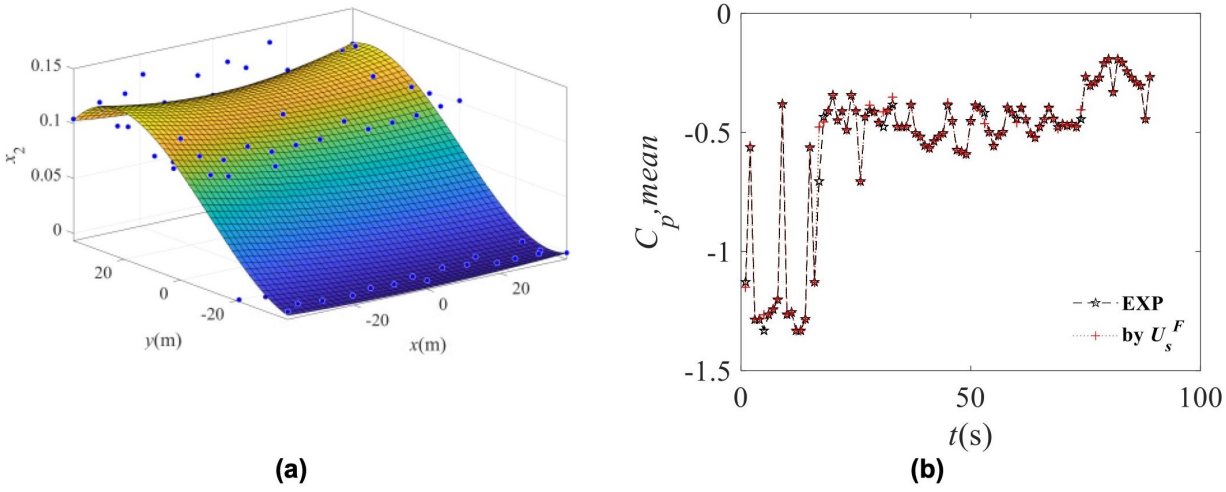

Figure 17: Example of spatial variation of coefficient x_1, Eq. (2), for the case G_1, $\theta = 0°$ (a) and comparison between $C_{p,mean}$ by experiments and by U^{S^F}

Quantities $x_{1,..4}$ in Eq. (2) were obtained for all geometries given in Table 1. The coefficients $x_{1,..4}$ of all the pressure taps illustrated in Figure 2 are fitted through a 95% level of confidence polynomial surface of degree two in x and degree three in y, according to:

$$x_i(x,y) = p_1 + p_2x + p_3y + p_4x^2 + p_5xy + p_6x^2 + p_7x^2y + p_8xy^2 + p_9x^3 \quad (10)$$

where $x_i(x,y)$ is the polynomial surface, $p_1, \ldots, p_9$ are the constants, and x and y are the centroid of each Thiessen polygon. An example of $x_i(x,y)$ is illustrated in Figure 17a for the case of geometry G_1, $\theta = 0°$.

The nine coefficients of the fitting polynomial for all four coefficients $x_{1,..4}$ defined in Eq. (6), for all geometries listed in Table 1 and all three wind angles investigated, are given in Appendix A.

The surrogated and fitted eigenvalues, U^{S^F}, the surrogated singular values S^S and the surrogated eigenvectors, V^S, are used to reconstruct the surrogated pressure coefficients time histories, ${C_p}^{S,F}$ according to Eq. (3) from which it is possible to recalculate mean pressure coefficients in accordance with the Principal Component Analysis (PCA) approach [44].

In this case, using only one pressure mode and a surrogated and fitted left singular vectors matrix, the difference between the mean experimental pressure coefficients and the mean surrogated pressure coefficients is smaller than 13% for all geometries and wind angles investigated. Table 3 gives the error in percentage for all geometries and wind angles investigated.

Table 3: Relative error in percentage between experimental values and by TSVD values

%	$\theta = 0°$	$\theta = 45°$	$\theta = 90°$
G_1	1.4	0.1	3.9
G_2	2.5	0.1	3.3
G_3	4.1	0.1	10.4
G_4	6.1	0.1	7.5
G_5	6.0	9.5	3.8
G_6	4.9	0.1	2.8
G_7	12.3	0.3	4.1
G_8	12.5	0.1	0.8

5 Mean pressure coefficients modification through upper pressure modes asymmetrical trends

The pressure modes distribution discussed in Section 3 can be considered as a synthetic spatial representation of the wind action on the roof and the singular values are the weights of each pressure mode. Even if pressure maps for mode #1 (Figures 8-11) shows a very similar trend to mean pressure coefficients (Figure 5), the upper modes show a different distribution, as illustrated in Figure 18.

Examples of upper pressure modes for geometry G_1 with $\theta = 0°$ are shown in Figure 18. For this specific geometry and wind angle, modes #3 and #5 are asymmetrical and mode #2 is diagonal. The modes variability is related to the time depending fluctuation of pressure coefficients. Comparing trends for all 20 modes (based on TSVD), it was observed that the majority of modes are asymmetric. This indicates that the asymmetrical pressure distribution of wind loads should be considered during the design. This contrasts with Codes, Standards and literature suggesting the use of the only symmetric distribution of pressure coefficients (Figure 5), [16–18].

For the case of cable nets and membrane roofs, asymmetrical load conditions represent the most severe load combination because the local instability can occur due to the unloading of the internal cable tension (Figure 19). For this reason, asymmetrical load combinations in the design phase are the worst scenario compared with symmetrical combinations.

In order to provide asymmetrical wind distributions, the proposed procedure consists in multiplying the pressure coefficients by normalized pressure modes.

Normalized upper modes were used to obtain asymmetrical pressure coefficients distribution, $C_{p,mean} \cdot \nu$, to estimate asymmetrical wind action load combinations. The

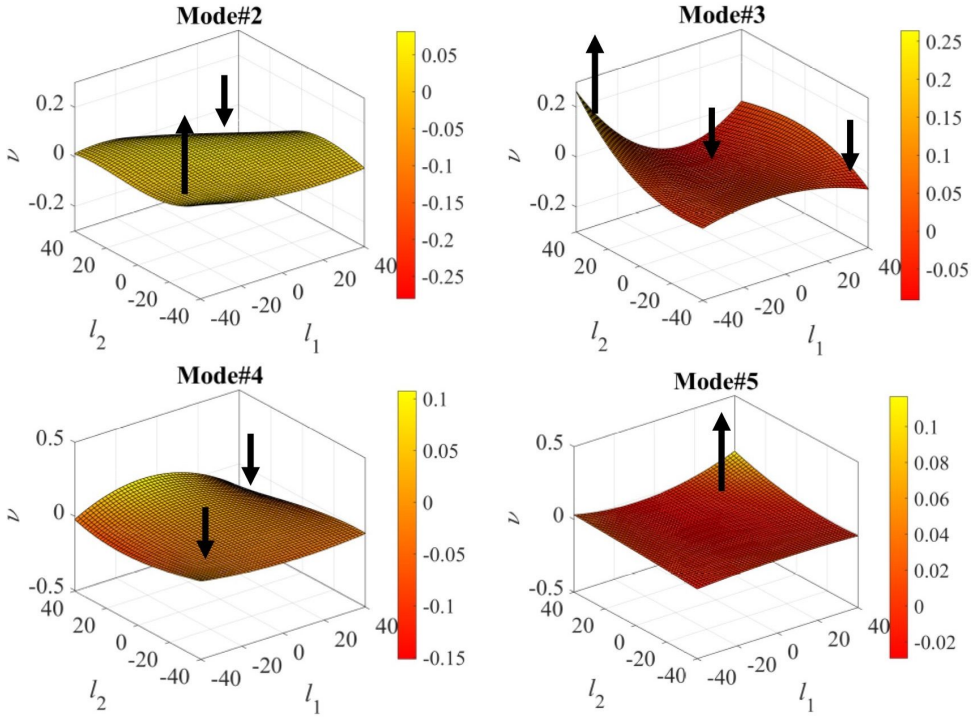

Figure 18: Examples of upper pressure modes for geometry G_1 with $\theta = 0°$. The black arrows indicate the upward or downward curvature

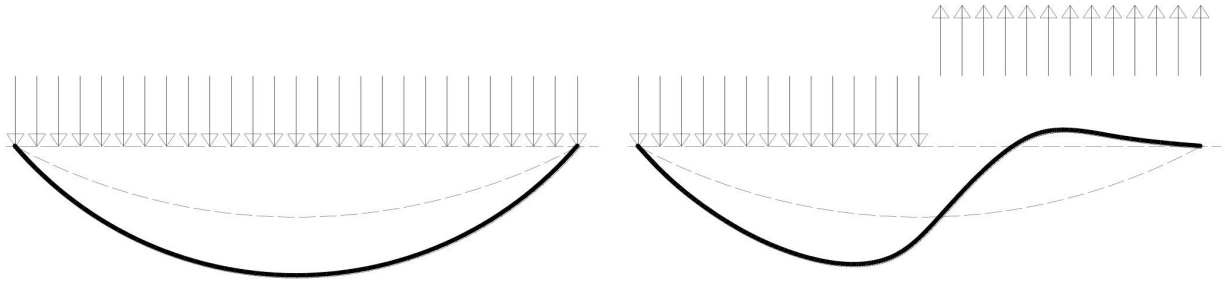

Figure 19: Cable deformation under uniformly and non-uniformly load distribution

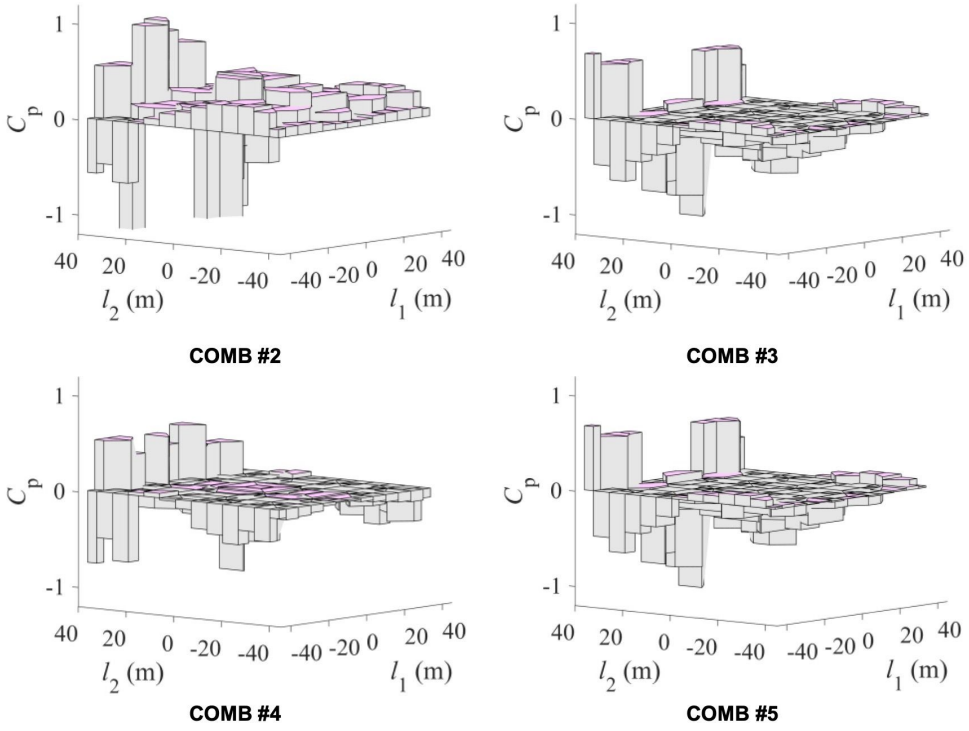

Figure 20: Examples of asymmetrical pressure coefficient combination, $C_{p,mean}v$, for geometry G_1 and $\theta = 0^\circ$

mean pressure coefficients calculated from the randomization of PSD (see Section 4.2) are used to provide asymmetrical combinations. Figure 20 shows some examples obtained by modes #2 - #5, for geometry G_1 and $\theta = 0^\circ$. Examples illustrated in Figure 20 show a non-uniformly distributed positive (*i.e.*, downward pressure) and negative (*i.e.*, upward pressure, suction) pressure coefficients.

6 FEM analyses

The case with geometry G_1 and $\theta = 0^\circ$ is used in the following to estimate the vertical displacements using a FEM model. The cable wheelbase, i, was assumed to be equal for the upward and downward cables and equal to 2 m. The upward and downward cable cross-sections were defined using the radii ϕ_1 and ϕ_2, respectively. Here, $\phi_1 = 0.02$ m and $\phi_1 = 0.01$ m are assumed. The cables have equivalent cable Young Modulus, E, equal to 1.65×10^5 MPa. The permanent load of the membrane was assumed to be 0.05 kN/m^2. The dead load owing to the cable weight was assumed equal to 0.1 kN/m^2.

The wind action using both envelope combinations (see Figure 13) and asymmetrical combinations (see Figure 20) was estimated as $W = 0.5\rho U^2 C_p$, where $\rho$is the air density assumed equal to 1.25 kg/m^2 and U is the wind velocity at the roof level. U is assumed equal to 30 m/s (*i.e.*, the maximum given by [19]).

Structural analyses were performed on the FEM model (Figure 21a) using TENSO [51] nonlinear geometrical analysis program. This software can execute a dynamic step-by-step integration of a nonlinear three-dimensional struc-

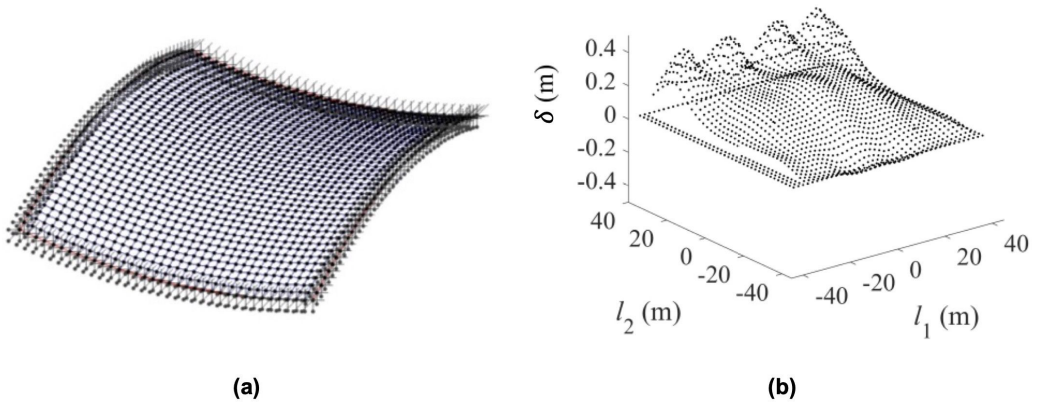

Figure 21: Cable net FEM analyses: FEM model (a), vertical displacements by using experimental mean pressure coefficients (b)

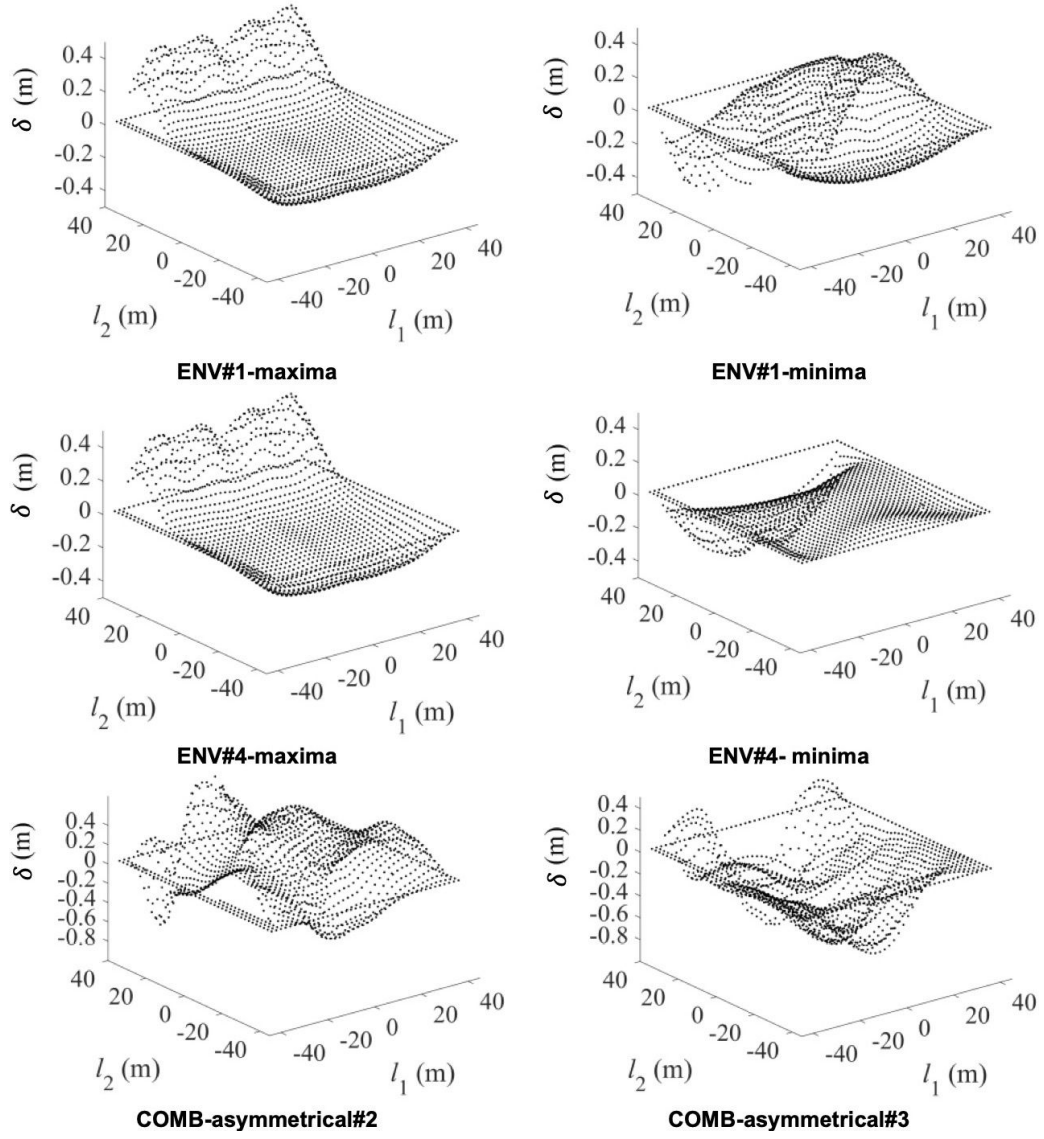

Figure 22: Cable net vertical displacements by FEM analyses by proposed pressure wind load combinations given by modified mean pressure coefficients trends

ture with geometric nonlinearities. The cables are discretized as straight cable segments. The global stiffness matrix is updated at each load step by assembling the stiffness sub-matrices of the elements, which are updated to consider the strain observed in the previous time step, thus accounting for geometric nonlinearity effects.

TENSO solves for the static equilibrium of the structure under dead, gravity, and construction loads (before wind loads application) by nonlinear static analysis. Two methods are used simultaneously: step-by-step incremental method and a 'subsequent interaction' method with variable stiffness matrix (secant method). The Newmark–Beta method with Rayleigh damping is used for numerical integration of the dynamic equations [51].

Figure 21 shows the static deformation of the cable net obtained by experimental mean pressure coefficients and Figure 22 shows results obtained by envelope and asymmetrical combinations.

Results show that envelope combinations obtained by minima pressure modes and asymmetrical combinations predict larger upward and downward displacements compared with the case when mean pressure coefficients are employed.

The maximum value of vertical displacement upward given by experimental mean pressure coefficients is about 0.4 m in the flow detachment zone. No significant downward vertical displacements are estimated using mean experimental values of pressure coefficients. Contrarily, the proposed envelope and asymmetrical distribution of pressure coefficients have given 0.6 m upward and 0.8 m downward.

These results highlight the importance of the use of the modified mean pressure coefficients in the design process to properly capture the displacements induced by the wind on hyperbolic paraboloid roofs. Besides, these results highlight the large underestimation in terms of displacements using mean pressure coefficients as commonly suggested by Standards and Codes of Practice.

7 Conclusions

A modification of mean pressure coefficients on hyperbolic paraboloid roofs was obtained from the SVD on data coming from wind tunnel tests. The proposed approach was applied on eight different geometries of buildings covered with a hyperbolic paraboloid shape with two different curvatures (*i.e.*, one flatter and one more curved), two different plan shape (*i.e.*, square and rectangular shape) and four different total height. The prototypes represent cable nets structure made of cables and a membrane. Three different wind angles were investigated, 0° (parallel to downward cables), 45°, and 90° (parallel to upward cables).

Experimental models were equipped with 89 (for square plan geometries) and 95 (for rectangular plan geometries) pressure taps. Singular values (*i.e.*, eigenvalues), left singular vectors and right singular vectors (*i.e.*, pressure modes) were estimated from wind pressure random processes measured from wind tunnel tests. For the cases investigated, twenty selected pressure modes are sufficient to reconstruct pressure coefficients time history with an error smaller than around 13%. The selected pressure modes were fitted through a polynomial surface. Normalized and fitted pressure modes were overlapped to obtain envelopes.

Surrogated mean pressure coefficients were estimated through randomization of the fitted Power Spectral Density (PSD) of the left singular vectors and they were multiplied by normalized envelope pressure modes to obtain envelope load combinations. Finally, asymmetrical upper-pressure modes were normalized and multiplied by surrogated mean pressure coefficients to obtain asymmetrical load combinations.

Finally, envelope and asymmetrical pressure coefficients were used to estimate wind loads combinations. Static FEM analyses were performed on a case of study to estimate vertical displacements. It was observed that upward vertical displacements induced by envelopes and asymmetrical load combinations are larger than values estimated using experimental mean pressure coefficients.

Conflict of Interests: The authors declare no conflict of interest regarding the publication of this paper.

References

[1] Vassilopoulou I., Petrini F., Gantes C.J., Nonlinear Dynamic Behavior of Cable Nets Subjected to Wind Loading, Structures, 2017 10, 170-183.

[2] Vassilopoulou I., Gantes C.J., Influence of a Deformable Contour Ring on the Nonlinear Dynamic Response of Cable Nets. Structures, 2016, 6, 146-158.

[3] Rizzo F., Zazzini P., Shape dependence of acoustic performances in buildings with a Hyperbolic Paraboloid cable net membrane roof, J. Acoust. Australia, 2017, 45 (2), 421-443.

[4] Rizzo F., Zazzini P., Improving the acoustical properties of an elliptical plan space with a cable net membrane roof, J. Acoust. Australia, 2016, 44, 449-456.

[5] Kawai H., Yoshie R., Wind-induced response of a large cantilevered roof., J. Wind Eng. Industr. Aerodyn., 1999, 83, 263-275.

[6] Letchford C.W., Killen G.P., Equivalent static wind loads for cantilevered grandstand roofs. Eng. Struct., 2002, 24(2), 207-217.
[7] Letchford C.W., Denoon R.O., Johnson G., Mallam A., Dynamic characteristics of cantilever grandstand roofs, Eng. Struct., 2002, 24(8), 1085-1090.
[8] Killen G.P., Letchford C.W., A parametric study of wind loads on grandstand roofs, Eng. Struct., 2001, 23(6), 725-735.
[9] Kimoto E., Kawamura S., Aerodynamic criteria of hanging roofs for structural Design, Proc. IASS Symposium, Osaka, 1986, 249-256.
[10] Kimoto E., Kawamura S., Aerodynamic behavior of one-way type hanging roofs, J. Wind Eng. Industr. Aerodyn., 1983, 13(1-3), 395-405.
[11] Zhang Z., Tamura Y., Wind Tunnel Test on Cable Dome of Geiger Type., J. Comput. Nonlin. Dyn., 2007, 2(3): 218-224.
[12] Forster B., Cable and membrane roofs, a historical survey, Struct. Eng. Rev.,1994, 6,3-5.
[13] Lewis W.J..Tension structures: form and behavior, Thomas Telford, London, 2003.
[14] Majowiecki M., Tensostrutture: Progetto e Verifica, Crea, Milano (in Italian), 2004.
[15] Novak M., Kassem M., Free Vibration of Light Roofs Backed by Cavities., J. Eng. Mech. Div., 1990, 116(3), 549-564.
[16] Rizzo F., D'Asdia P., Lazzari M., Procino L., Wind action evaluation on tension roofs of hyperbolic paraboloid shape, Eng. Struct., 2011, 33 (2), 445-461.
[17] Rizzo F., Barbato M., Sepe V., 2018. Peak factor statistics of wind effects for hyperbolic paraboloid roofs, Eng. Struct., 173, 313-330.
[18] Rizzo F., Sepe V., Ricciardelli F., Avossa A. M., Wind pressures on a large span canopy roof, Wind Struct., 2020, 30(2): 299-316.
[19] CNR (National Research Council of Italy), CNR-DT207/2018, Guide for the Assessment of Wind Actions and Effects on Structures, 2018.
[20] AIJ (Architectural Institute of Japan), Recommendations for Loads on Buildings, Chapter 6: Wind Loads, 2004.
[21] ASCE (American Society of Civil Engineering), Wind tunnel studies of buildings and structures, N. Isyumov, Ed., Manuals of Practice (MOP) 67, 1999.
[22] ASCE (American Society of Civil Engineering), Minimum Design Loads for Buildings and Other Structures, ASCE 7:2010, 2010.
[23] AS/NZS (Standards Australia / Standards New Zealand), Structural design actions; Part 2: Wind actions. AS/NZS 1170.2:2002, 2011.
[24] NRC/CNRC (National Research Council / Conseil National de Recherches Canada), Commentary to the National Building Code of Canada, Commentary I: Wind Load and Effects, 2010.
[25] CEN (Comité Européen de Normalization), Eurocode 1: Actions on structures – Part 1-4: General actions - Wind actions, EN-1991-1-4, 2005.
[26] Australian/New Zealand Standard, Structural design actions; Part 2: Wind actions, AS/NZS 1170.2:2002.C.W, 2002.
[27] Krishna P., Kumar K., Bhandari N.M., Wind Loads on Buildings and Structures. Indian Standard IS:875, Part 3, Proposed Draft & Commentary, Bendat, J.S., Piersol, A.G., 2000. Random data analysis and measurement procedures, (3rd edition). John Wiley and Sons, New York, NY, USA, 2012.
[28] CEN (Comité Européen de Normalization). EN1991-1-4: Eurocode1: Actions on structures - Part 1-4: General actions - Wind actions, 2005.
[29] SIA (Swiss Society of Engineers and Architects). Action on structures – Appendix C: Force and pressure factors for wind, SIA 261:2003, 2003.
[30] Ueda H., Hibi K., Tamura Y., Fujii K., Multi-channel simultaneous fluctuating pressure measurement system and its application., J. Wind Eng. Industr. Aerodyn., 1994, 51, 1, 93-104.
[31] Holmes, J. D., Analysis and synthesis of pressure fluctuations on bluff bodies using eigenvectors., J. Wind Eng. Industr. Aerodyn., 1990, 33, 219-230.
[32] Tamura Y., Kareem E. A., CERMAK, J. E., Pressure fluctuations on a square building mode in boundary-layer flows., J. Wind Eng. Industr. Aerodyn., 1984 16, 17-41.
[33] Cook N.J., Mayne J.R., A novel working approach to the assessment of wind loads for equivalent static design., J. Wind Eng. Industr. Aerodyn., 1979, 4(2), 149-164.
[34] Cook N.J., Mayne J.R., A refined working approach to the assessment of wind loads for equivalent static design, J. Wind Eng. Industr. Aerodyn., 1980, 6(1-2), 125-137.
[35] Cook N.J., Calibration of the quasi-static and peak-factor approaches to the assessment of wind loads against the method of Cook and Mayne., J. Wind Eng. Industr. Aerodyn., 1982, 10(3), 315-341.
[36] Cook N.J., The designer's guide to wind loading of building structures, Part 1: Background, damage survey, wind data and structural classification, Building Research Establishment, Butterworths, U.K, 1985.
[37] Cook N.J., The designer's guide to wind loading of building structures, Part 2: Static structures, Building Research Establishment, Butterworths, U.K, 1990.
[38] Tamura Y., Yoshida A., Zhang L., Ito T., Nakata S., Examples of modal identification of structures in Japan by FDD and MRD techniques. Proceedings of the EACWE4 — The Fourth European & African Conference on Wind Engineering J. Naprstek & C. Fischer (eds); ITAM AS CR, Prague, 11-15 July, 2005.
[39] Tamura Y., Ueda H., Kikuchi H., Hibi K., Suganuma S., Bienkiewicz B., Proper orthogonal decomposition study of approach wind-building pressure correlation, In: Proc. Ninth Int. Conf. Wind Eng., Retrospect and Prospect, 1995, (4), 2115-2126.
[40] Tamura Y., An introduction of applying proper orthogonal decomposition to random fields, J. Wind Eng., Trans. Japan Assoc. Wind Eng., 1995, 65, 33-41 (in Japanese).
[41] Bienkiewicz B., Ham H.J., Proper orthogonal decomposition of roof pressure., J. Wind Eng. Industr. Aerodyn., 1993, 50, 193-202.
[42] Bienkiewicz B., Tamura Y., Ham H.J., Ueda H., Hibi K., Proper orthogonal decomposition and reconstruction of multi-channel roof pressure., J. Wind Eng. Industr. Aerodyn., 1995, 54-55, 369-381.
[43] Kikuchi H., Tamura Y., Ueda H., Hibi K., Dynamic wind pressures acting on a tall building model proper orthogonal decomposition., J. Wind Eng. Industr. Aerodyn., 1997, 69-71, 631-646.
[44] Armitt J., Eigenvector analysis of pressure fluctuations on the West Burton instrumented cooling tower, Central Electricity Research Laboratories (U.K.) Internal Report RD/L/N 114/68, 1968.
[45] Best R.J., Holmes J.D., Use of eigenvalues in the covariance integration method for determination of wind load elects., J. Wind Eng. Industr. Aerodyn., 1983, 13, 359-370.
[46] Matlab software, Mathwork documentation, https://www.mathworks.com/help/matlab/, 2019.
[47] Holmes J.D., Optimised peak load distributions., J. Wind Eng. Industr. Aerodyn., 1992, 41-44, 267-276.

[48] Holmes J.D., Denoon R., Kwok K.C.S., Glanville M.J., Wind loading and response of large stadium roofs, In: Proc. of the IASS Int. Symp. Shell and Spatial Structures, Singapore, 10-14 November 1997, 317-324.

[49] Isyumov N., Poole M., Wind induced torque on square and rectangular building shapes., J. Eng. Industr. Aerodyn., 1984, 13, 183-196.

[50] Lee B.E., The elects of turbulence on the surface pressure field of a square prism, J. Fluid Mech., 1975, 69, 263-282.

[51] Rizzo F., Caracoglia L., Artificial Neural Network model to predict the flutter velocity of suspension bridges, Comp. Struct., 2020, 233, 106236.

A Appendix A

The nine coefficients of the fitting polynomial for all four coefficients $x_{1,..4}$ defined in Eq. (6) are given in Tables A4 and A5 for square plan models and rectangular plan models, respectively, for all geometries and all three wind angles investigated.

Table A4: Polynomial surface fitting coefficients (*i.e.*, $\cdot 10^{-3}$) for square plan geometry

	G_1											
	$\theta = 0°$				$\theta = 45°$				$\theta = 90°$			
	x_1	x_2	x_3	x_4	x_1	x_2	x_3	x_4	x_1	x_2	x_3	x_4
p_1	0.4	90.9	−0.4	92.1	0.5	117.1	−0.5	72.0	0.2	65.3	−0.2	203.6
p_2	0.0	0.1	0.0	−0.8	0.0	0.0	0.0	−0.2	0.0	0.0	0.0	−3.2
p_3	0.0	2.5	0.0	0.1	0.0	0.1	0.0	−1.8	0.0	2.9	0.0	−13.2
p_4	0.0	0.0	0.0	0.1	0.0	0.0	0.0	0.0	0.0	0.0	0.0	0.0
p_5	0.0	0.0	0.0	−0.1	0.0	0.0	0.0	0.0	0.0	0.0	0.0	0.1
p_6	0.0	0.0	0.0	0.1	0.0	0.0	0.0	0.1	0.0	0.0	0.0	0.1
p_7	0.0	0.0	0.0	0.0	0.0	0.0	0.0	0.0	0.0	0.0	0.0	0.0
p_8	0.0	0.0	0.0	0.0	0.0	0.0	0.0	0.0	0.0	0.0	0.0	0.0
p_9	0.0	0.0	0.0	0.0	0.0	0.0	0.0	0.0	0.0	0.0	0.0	0.0
	G_2											
	$\theta = 0°$				$\theta = 45°$				$\theta = 90°$			
	x_1	x_2	x_3	x_4	x_1	x_2	x_3	x_4	x_1	x_2	x_3	x_4
p_1	0.3	82.0	−0.3	190.5	0.4	94.9	−0.4	64.8	0.3	90.5	−0.3	72.7
p_2	0.0	−0.3	0.0	1.1	0.0	0.1	0.0	−0.5	0.0	−0.3	0.0	0.3
p_3	0.0	0.6	0.0	15.6	0.0	0.0	0.0	0.5	0.0	1.7	0.0	−0.2
p_4	0.0	0.0	0.0	0.0	0.0	0.0	0.0	0.0	0.0	0.0	0.0	0.1
p_5	0.0	0.0	0.0	0.1	0.0	0.0	0.0	−0.1	0.0	0.0	0.0	0.0
p_6	0.0	0.0	0.0	0.1	0.0	0.0	0.0	0.1	0.0	0.0	0.0	0.1
p_7	0.0	0.0	0.0	0.0	0.0	0.0	0.0	0.0	0.0	0.0	0.0	0.0
p_8	0.0	0.0	0.0	0.0	0.0	0.0	0.0	0.0	0.0	0.0	0.0	0.0
p_9	0.0	0.0	0.0	0.0	0.0	0.0	0.0	0.0	0.0	0.0	0.0	0.0
	G_3											
	$\theta = 0°$				$\theta = 45°$				$\theta = 90°$			
	x_1	x_2	x_3	x_4	x_1	x_2	x_3	x_4	x_1	x_2	x_3	x_4
p_1	0.3	89.9	−0.3	208.3	0.3	96.1	−0.3	147.9	0.2	48.0	−0.2	87.8
p_2	0.0	−0.3	0.0	−1.3	0.0	0.0	0.0	−4.3	0.0	−0.6	0.0	1.7
p_3	0.0	1.1	0.0	4.6	0.0	−0.1	0.0	2.9	0.0	3.2	0.0	−1.8
p_4	0.0	0.0	0.0	−0.1	0.0	0.0	0.0	0.0	0.0	0.0	0.0	0.1
p_5	0.0	0.0	0.0	0.0	0.0	0.0	0.0	0.0	0.0	0.0	0.0	0.0
p_6	0.0	0.0	0.0	0.1	0.0	0.0	0.0	0.0	0.0	0.0	0.0	0.2
p_7	0.0	0.0	0.0	0.0	0.0	0.0	0.0	0.0	0.0	0.0	0.0	0.0
p_8	0.0	0.0	0.0	0.0	0.0	0.0	0.0	0.0	0.0	0.0	0.0	0.0
p_9	0.0	0.0	0.0	0.0	0.0	0.0	0.0	0.0	0.0	0.0	0.0	0.0
	G_4											
	$\theta = 0°$				$\theta = 45°$				$\theta = 90°$			
	x_1	x_2	x_3	x_4	x_1	x_2	x_3	x_4	x_1	x_2	x_3	x_4
p_1	0.3	87.7	−0.3	121.2	0.3	95.0	−0.3	90.6	0.0	0.0	0.0	0.0
p_2	0.0	−0.3	0.0	−0.9	0.0	0.0	0.0	0.1	0.0	0.0	0.0	0.0
p_3	0.0	2.2	0.0	0.6	0.0	0.2	0.0	−1.2	0.0	0.0	0.0	0.0
p_4	0.0	0.0	0.0	0.0	0.0	0.0	0.0	0.0	0.0	0.0	0.0	0.0
p_5	0.0	0.0	0.0	−0.1	0.0	0.0	0.0	0.0	0.0	0.0	0.0	0.0
p_6	0.0	0.0	0.0	0.1	0.0	0.0	0.0	0.1	0.0	0.0	0.0	0.0
p_7	0.0	0.0	0.0	0.0	0.0	0.0	0.0	0.0	0.0	0.0	0.0	0.0
p_8	0.0	0.0	0.0	0.0	0.0	0.0	0.0	0.0	0.0	0.0	0.0	0.0
p_9	0.0	0.0	0.0	0.0	0.0	0.0	0.0	0.0	0.0	0.0	0.0	0.0

Table A5: Polynomial surface fitting coefficients (*i.e.*, $\cdot 10^{-3}$) for rectangular plan geometry

					G_5							
	$\theta = 0°$				$\theta = 45°$				$\theta = 90°$			
	x_1	x_2	x_3	x_4	x_1	x_2	x_3	x_4	x_1	x_2	x_3	x_4
p_1	0.3	47.6	−0.3	140.2	0.4	90.3	−0.4	133.3	0.3	88.2	−0.3	37.9
p_2	0.0	−0.4	0.0	1.8	0.0	−0.1	0.0	−8.3	0.0	−0.4	0.0	−3.2
p_3	0.0	2.9	0.0	−4.9	0.0	−0.3	0.0	19.5	0.0	1.6	0.0	5.1
p_4	0.0	0.0	0.0	−0.1	0.0	0.0	0.0	0.1	0.0	0.0	0.0	−0.1
p_5	0.0	0.0	0.0	0.1	0.0	0.0	0.0	−0.6	0.0	0.0	0.0	−0.3
p_6	0.0	0.0	0.0	0.1	0.0	0.0	0.0	0.2	0.0	0.0	0.0	0.4
p_7	0.0	0.0	0.0	0.0	0.0	0.0	0.0	0.0	0.0	0.0	0.0	0.0
p_8	0.0	0.0	0.0	0.0	0.0	0.0	0.0	0.0	0.0	0.0	0.0	0.0
p_9	0.0	0.0	0.0	0.0	0.0	0.0	0.0	0.0	0.0	0.0	0.0	0.0
					G_6							
	$\theta = 0°$				$\theta = 45°$				$\theta = 90°$			
	x_1	x_2	x_3	x_4	x_1	x_2	x_3	x_4	x_1	x_2	x_3	x_4
p_1	0.3	87.7	−0.3	121.2	0.3	95.0	−0.3	90.6	0.0	0.0	0.0	0.0
p_2	0.0	−0.3	0.0	−0.9	0.0	0.0	0.0	0.1	0.0	0.0	0.0	0.0
p_3	0.0	2.2	0.0	0.6	0.0	0.2	0.0	−1.2	0.0	0.0	0.0	0.0
p_4	0.0	0.0	0.0	0.0	0.0	0.0	0.0	0.0	0.0	0.0	0.0	0.0
p_5	0.0	0.0	0.0	−0.1	0.0	0.0	0.0	0.0	0.0	0.0	0.0	0.0
p_6	0.0	0.0	0.0	0.1	0.0	0.0	0.0	0.1	0.0	0.0	0.0	0.0
p_7	0.0	0.0	0.0	0.0	0.0	0.0	0.0	0.0	0.0	0.0	0.0	0.0
p_8	0.0	0.0	0.0	0.0	0.0	0.0	0.0	0.0	0.0	0.0	0.0	0.0
p_9	0.0	0.0	0.0	0.0	0.0	0.0	0.0	0.0	0.0	0.0	0.0	0.0
					G_7							
	$\theta = 0°$				$\theta = 45°$				$\theta = 90°$			
	x_1	x_2	x_3	x_4	x_1	x_2	x_3	x_4	x_1	x_2	x_3	x_4
p_1	0.4	51.4	−0.4	75.8	0.4	92.4	−0.4	106.5	0.3	57.5	−0.3	81.1
p_2	0.0	−0.5	0.0	2.9	0.0	−0.2	0.0	2.5	0.0	−0.3	0.0	−0.4
p_3	0.0	2.8	0.0	−2.4	0.0	−0.5	0.0	4.7	0.0	2.8	0.0	−2.9
p_4	0.0	0.0	0.0	0.2	0.0	0.0	0.0	0.1	0.0	0.0	0.0	0.0
p_5	0.0	0.0	0.0	−0.1	0.0	0.0	0.0	0.2	0.0	0.0	0.0	−0.1
p_6	0.0	0.0	0.0	0.1	0.0	0.0	0.0	0.1	0.0	0.0	0.0	0.2
p_7	0.0	0.0	0.0	0.0	0.0	0.0	0.0	0.0	0.0	0.0	0.0	0.0
p_8	0.0	0.0	0.0	0.0	0.0	0.0	0.0	0.0	0.0	0.0	0.0	0.0
p_9	0.0	0.0	0.0	0.0	0.0	0.0	0.0	0.0	0.0	0.0	0.0	0.0
					G_8							
	$\theta = 0°$				$\theta = 45°$				$\theta = 90°$			
	x_1	x_2	x_3	x_4	x_1	x_2	x_3	x_4	x_1	x_2	x_3	x_4
p_1	0.3	58.0	−0.3	56.5	0.4	91.0	−0.4	111.8	0.4	86.5	−0.4	141.9
p_2	0.0	−0.3	0.0	−11.9	0.0	0.2	0.0	0.5	0.0	−0.4	0.0	−1.9
p_3	0.0	2.8	0.0	6.6	0.0	0.1	0.0	2.0	0.0	2.0	0.0	0.4
p_4	0.0	0.0	0.0	−0.9	0.0	0.0	0.0	0.0	0.0	0.0	0.0	−0.1
p_5	0.0	0.0	0.0	−0.8	0.0	0.0	0.0	0.1	0.0	0.0	0.0	0.0
p_6	0.0	0.0	0.0	0.7	0.0	0.0	0.0	0.0	0.0	0.0	0.0	0.1
p_7	0.0	0.0	0.0	0.1	0.0	0.0	0.0	0.0	0.0	0.0	0.0	0.0
p_8	0.0	0.0	0.0	0.0	0.0	0.0	0.0	0.0	0.0	0.0	0.0	0.0
p_9	0.0	0.0	0.0	0.0	0.0	0.0	0.0	0.0	0.0	0.0	0.0	0.0